An optimal control method of internal resonances for vibration isolation system using an aperiodic isolator

Yujun Liu[1], Jing Liu[1,2*], Guang Pan[1,2], Qiaogao Huang[1,2], and Baowei Song[1,2]

[1] *School of Marine Science and Technology, Northwestern Polytechnical University, Xi'an 710072, China;*

[2] *Key Laboratory of Unmanned Underwater Vehicle, Northwestern Polytechnical University, Xi'an 710072, China*

Periodic isolator is well known for its wave filtering characteristic. While in middle and high frequencies, the internal resonances of the periodic isolator are evident especially when damping is small. This study proposes a novel aperiodic vibration isolation for improving the internal resonances control of the periodic isolator. The mechanism of the internal resonances control by the aperiodic isolator is firstly explained. For comparing the internal resonances suppression effect of the aperiodic isolator with the periodic isolator, a dynamic model combing the rigid machine, the isolator, and the flexible plate is derived through multi subsystem modeling method and transfer matrix method, whose accuracy is verified through the finite element method. The influences of the aperiodicity and damping of the isolator on the vibration isolation performance and internal resonances suppression effect are investigated by numerical analysis. The numerical results demonstrate that vibration attenuation performances of the periodic isolator and aperiodic isolator are greatly over than that of the continuous isolator in middle and high frequencies. The aperiodic isolator opens the stop bandgaps comparing with the periodic isolator where the pass bandgaps are periodically existed. The damping of the isolator has the stop bandgap widening effect on both the periodic isolator and the aperiodic isolator. In addition, a parameter optimization algorithm of the aperiodic isolator is presented for improving the internal resonances control effect. It is shown that the vibration peaks within the target frequency band of the aperiodic isolator are effectively reduced after the optimization. Finally, the experiments of the three different vibration isolation systems are conducted for verifying the analysis work.

Internal resonances, Vibration isolation, Periodic structure, Vibration wave propagation

1.   Introduction

Vibration isolation technology is commonly utilized in engineering for vibration suppression. A vibration isolator is a resilient component connecting the machine and the foundation, reducing the mechanical vibration energy transmitted to the foundation by regulating the dynamic parameters of the isolator. The review [1] on the design and application of the vibration isolator showed that the ideal vibration isolator could reduce the vibration at a rate of 12 dB per octave within the isolation frequency band, based on the assumption that the isolator is a massless spring element. In real application, vibration isolator could hardly meet the requirement of vibration control in high frequency due to the mass effect of the realistic isolator [2] and the elasticity of the flexible foundation [3-7]. The internal resonance [8] generated from the mass effect [9] of a realistic vibration isolator is also called wave effect. The influences of internal resonances on the vibration transmissibility of the isolation system are critical, that cause 20-30 dB increase in the vibration transmission and sound radiation at the internal resonance frequencies [10-12]. The high frequency vibration could be reduced by inserting an intermediate mass in the isolator, which is wildly known [13,14] in vibration isolation technology. Compared with single-layer isolators, double-layer isolators could reduce the vibration at a rate of 24 dB

per octave within the isolation frequency band.

The application of periodic structure (also called meta-material) achieves the notable physical characteristic like pass bandgap and stop bandgap [15]. Researchers [16] found that in the stop bandgap, the wave propagation direction is perpendicular to the incident direction, where the mode is antisymmetric and the wave cannot be excited in the response spectrum. The artificially designed periodic structures could regulate stop bandgap by adjusting the materials and geometries of periodic cells. According to the theory of the periodic structure, the wave could be attenuated exponentially in the stop bandgap and be propagated in the pass bandgap. The concept of introducing the periodic structure theory to the vibration isolator is available. The periodic vibration isolators have been designed in the form of periodic layered isolators [17,18], rods and beams with periodic insertions [19,20], and lattice structures [21-23]. These researches showed that a periodic vibration isolation system could greatly improve the isolation performance due to its special stop bandgap characteristics. However, the periodic structure is ineffective on the control of the internal resonances.

The effective control of the internal resonances could decline the vibration transmission and sound radiation. For reducing the impact of the internal resonances on the vibration transmission and sound radiation from the vibration isolation system, scholars present several control methods [24-27], such as isolators with additional vibration absorbers and active-passive isolation control. Sun et al. [24] presented a vibration isolator with a pivot arm to reduce the internal resonances from suspension of rail vehicles, which based on the mechanism of using an arm to provide a reaction force to offset the internal resonances. Du et al. [25] proposed a method to suppress the internal resonances of the vibration isolator utilizing passive and hybrid dynamic vibration absorbers. Dylejko et al. [26] investigated the application effect of transmission absorbers instead of vibration absorbers to minimize the internal resonances with the optimization method. Their results showed that the transmission absorbers could effectively decrease the vibration transmissibility at internal resonance frequencies. Most previous methods to control the internal resonances are proposed based on generating a negative force to offset the internal resonances. The combination of the above internal resonances control method and periodic vibration isolation system is complex. To overcome this problem, a simple isolator design to control the internal resonances based on the periodic isolator is required.

This study proposes a novel aperiodic vibration isolator with the aim of reducing internal resonances. Firstly, the mechanism of the internal resonances control by the aperiodic isolator is demonstrated. The dynamic vibration isolation model combining the rigid mass, the aperiodic

isolator, and the flexible foundation is established through the subsystem method and the transfer matrix method. Finite element models of the three vibration isolation systems are developed for validating the reliability of the proposed numerical method. The power flows of the vibration isolation systems and the real part of the transfer constants of the isolators are calculated and compared. For improving the internal resonances control effect, an optimization algorithm based on the particle swarm optimization (PSO) method is designed to optimize the lengths of the aperiodic isolator. The internal resonances control effect of the optimization algorithm on the designed aperiodic isolator is studied. Finally, vibration isolation experiments are carried out and discussed.

2. Theory

In this section, a type of aperiodic isolator consisting unequal-length metal rod and unequal-length rubber rod is designed. The concept of using the aperiodic isolator to suppress the internal resonances of the vibration isolation system is demonstrated. The dynamic model of the aperiodic vibration isolation system with supporting plate is established.

2.1 Aperiodic isolator

This study proposes an aperiodic vibration isolator based on one kind of design of periodic isolator [26]. Figure 1 shows the structure design diagrams of the different vibration isolators, which respectively are the continuous isolator (Fig. 1a), the periodic isolator (Fig. 1b), and the aperiodic isolator (Fig. 1c). Figure 1a is a commonly used continuous isolator which is a resilient mounting made of rubber material. Figure 1b is a periodic isolator. The design idea of periodic isolator is connecting equal intermediate mass elements and equal resilient elements in series. This kind of periodic isolator is similar with the isolator with intermediate masses, which has been proposed to strengthen the high frequency vibration isolation performance [27]. Figure 1c is an aperiodic vibration isolator. The difference between the aperiodic vibration isolator and the periodic vibration
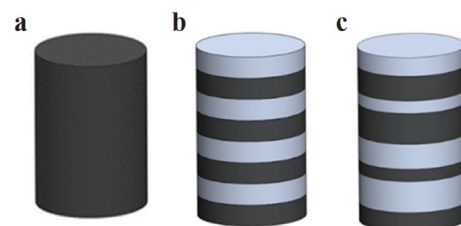

Figure 1 Structure design of **a** continuous isolator, **b** periodic isolator, and **c** aperiodic isolator.

isolator is that aperiodic vibration isolator combines unequal intermediate mass elements and unequal resilient elements. In the design of the periodic isolator and the aperiodic isolator, the resilient element and the intermediate mass element are respectively designed as rubber rod and the metal rod.

2.2 Internal resonances suppression by aperiodic isolator

The previous researches mainly focus on the vibration isolation ability of the periodic vibration isolator system. The periodic vibration isolator has a given frequency range stop bandgap, which attenuates wave propagation in the stop bandgap. However, the stop bandgaps of the periodic isolator are interrupted as the internal resonances occur, where the pass bandgaps exist. The study proposes an idea to expand the stop bandgaps by bonding different unit cells in series to form an aperiodic isolator. The material and geometrical parameters in each unit cell of the aperiodic isolator are different. As the internal resonances of the isolator diminish due to the diversification of the standing wave in the aperiodic isolator, the stop bandgap of the isolator would be broadened.

Figure 2 schematically shows periodic isolator, aperiodic isolator and their corresponding longitudinal standing wave in each isolator. The longitudinal standing wave effect in the rod element is associated with the longitudinal length and material according to the classical mechanical wave theory. In Fig. 2, there are only two kinds wavelength standing waves in the periodic isolator as it has equal metal rods and rubber rods, and multiple kinds wavelength standing waves in the aperiodic isolator as it has varied metal rods and rubber rods. The standing wave effect causes the internal resonances in vibration response of the isolator. The internal resonances' energy in the vibration response of the aperiodic isolator is dispersed at different frequencies as the number of the standing wave are increased. Hence, the periodic isolator generates unwanted internal resonances. This problem could be overcome by the aperiodic isolator.
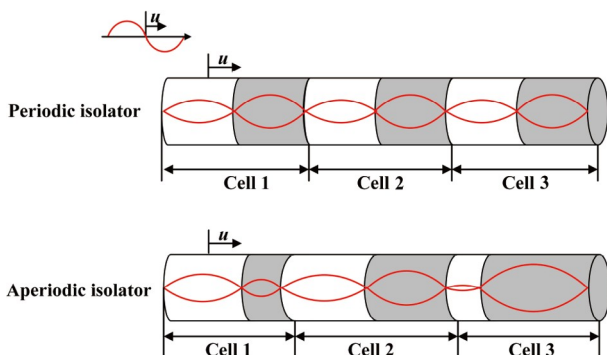
Figure 3 respectively shows the physical models of the periodic isolator and the aperiodic isolator consisting the machine, the isolator and the flexible supporting. The physical model of the periodic isolator in Fig. 3a is composed of the same mass units with parameters (A_1, E_1, h_1, ρ_1) and the same elastic units with parameters (A_2, E_2, H_2, ρ_2). Figure 3b shows the physical model of an aperiodic vibration isolator, where the isolation unit has varied mass units and elastic units with parameters (A_i, E_i, h_i, ρ_i).

The longitudinal motion equation of a single continuous rod [28] with density of ρ and complex Young's modulus of E^* is

$$\frac{\partial^2}{\partial x^2}u(x,t) - \frac{\rho}{E^*}\frac{\partial^2}{\partial t^2}u(x,t) = 0, \tag{1}$$

where $u(x,t)$ is the displacement amplitude of longitudinal wave, and complex Young's modulus of E^* is

$$E^* = E(1+\mathrm{i}\xi), \tag{2}$$

where ξ is the loss factor. The Voigt material damping model is used as viscoelastic damping model in the rubber and metal components. As shown in Eq. (2), the real part represents elastic property, and the imaginary part represents damping property. Considering a separating variables solution of Eq. (1) as $u(x,t) = U(x)\mathrm{e}^{\mathrm{i}\omega t}$, ω is the angular frequency. The longitudinal motion equation of the continuous rod in the separating variables form is given as

$$U(x) + k^2 U(x) = 0, \tag{3}$$

where k is the longitudinal wave number expressed as $k = \omega/\sqrt{E^*/\rho}$; the solution $U(x)$ could be written in the form of the superposition of wave traveling along $+x$ direction and wave traveling along $-x$ direction as $U(x) = U_1\mathrm{e}^{-\mathrm{i}kx} + U_2\mathrm{e}^{\mathrm{i}kx}$.

The longitudinal wave propagation characteristic of the continuous rod in the transfer matrix form is defined as

Figure 2 Longitudinal standing wave phenomenon in the periodic isolator and the aperiodic isolator.
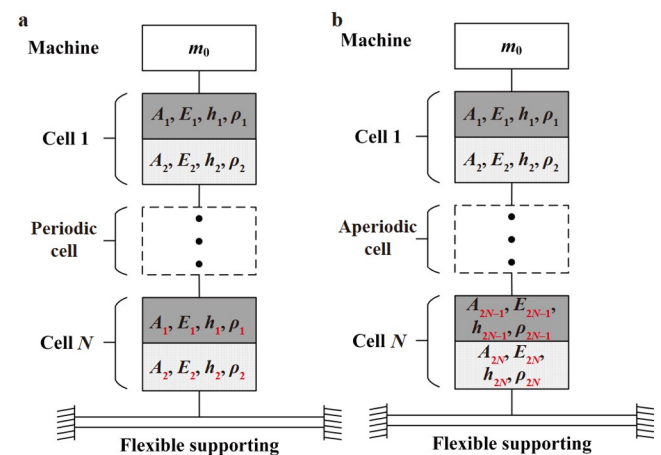

Figure 3 Dynamic models for **a** the periodic isolator and **b** the aperiodic isolator.

$$\begin{Bmatrix} F_L \\ F_R \end{Bmatrix} = \mathbf{K} \begin{Bmatrix} U_L \\ U_R \end{Bmatrix} = \begin{bmatrix} k_{11} & k_{12} \\ k_{21} & k_{22} \end{bmatrix} \begin{Bmatrix} U_L \\ U_R \end{Bmatrix}, \tag{4}$$

where U_L and U_R are the displacements of the left and right ends of the rod, respectively; F_L and F_R are the forces of the left and right ends of the rod. As the longitudinal length of the rod is L, the displacement of the boundary condition is defined as $U_L = U (x = 0)$ and $U_R = U (x = L)$. According to reciprocity and symmetry, $k_{11} = k_{22}$ and $k_{12} = k_{21}$ are required. The definition of the stiffness of the rod is the ratio of force to displacement of the rod, through fixing the displacement of one end of the rod, as $U_R = 0$ and $U_L = \Delta u$. The stiffnesses are defined as

$$k_{11} = \frac{F_L}{\Delta U}, \tag{5}$$

$$k_{12} = \frac{F_R}{\Delta U}. \tag{6}$$

The force of the rod is

$$F = EA \frac{\partial U}{\partial x}. \tag{7}$$

The displacement boundary conditions are

$$U_L = U_1 + U_2, \tag{8}$$

$$U_R = U_1 e^{-ikL} + U_2 e^{ikL} = 0. \tag{9}$$

By inserting Eqs. (7)-(9), the dynamic stiffness matrix $\mathbf{K}$ of the rod gives

$$\begin{bmatrix} k_{11} & k_{12} \\ k_{21} & k_{22} \end{bmatrix} = \frac{EA}{L} \begin{bmatrix} \dfrac{(1 - e^{-4ikL})ikL}{(1 - e^{-2ikL})^2} & \dfrac{2e^{-3ikL}(1 - e^{2ikL})ikL}{(1 - e^{-2ikL})^2} \\ \dfrac{2e^{-3ikL}(1 - e^{2ikL})ikL}{(1 - e^{-2ikL})^2} & \dfrac{(1 - e^{-4ikL})ikL}{(1 - e^{-2ikL})^2} \end{bmatrix}, \tag{10}$$

where L is the longitudinal length. Rearrange Eq. (4) and redescribe the dynamic motion in transferring the state variable of the left end of the rod U_L and F_L to that of the right end of the rod U_R and F_R by the transfer matrix $\mathbf{T}$, which is defined as

$$\begin{Bmatrix} U_R \\ F_R \end{Bmatrix} = \mathbf{T} \begin{Bmatrix} U_L \\ F_L \end{Bmatrix} = \begin{bmatrix} t_{11} & t_{12} \\ t_{21} & t_{22} \end{bmatrix} \begin{Bmatrix} U_L \\ F_L \end{Bmatrix}, \tag{11}$$

where $t_{11} = -k_{12}^{-1} k_{11}$, $t_{12} = -k_{12}^{-1}$, $t_{21} = -k_{22} k_{21}^{-1} k_{11}$, $t_{22} = k_{22} k_{12}^{-1}$.

Considering the aperiodic rods composing N rods, the transfer matrix $\mathbf{T}_t$ is the product of the transfer matrix of each rod, given as

$$\mathbf{T}_t = \mathbf{T}_1 \mathbf{T}_2 \cdots \mathbf{T}_N. \tag{12}$$

The eigenvalues λ of transfer matrix $\mathbf{T}_t$ represent the state variable transfer ratio on both sides of the aperiodic rods. The wave propagation characteristic is associated with the eigenvalues of the transfer matrix. When the wave transfer in structure, it has two results. One is transfer without at-

tenuation, and the other is transfer with attenuation. The case $\lambda = 1$ denotes that the state variables of the left and right ends of the rod have identical magnitude, which represents the pass bandgap with no wave attenuation. The opposite case $\lambda \neq 1$ denotes that the state variables of the left and right ends of the rod have different magnitudes. For the case $\lambda < 1$ signify wave attenuates in the forward direction. For the case $\lambda > 1$ signify wave attenuates in the backward direction [29]. λ can be defined as

$$\lambda = e^{\mu} = e^{\alpha + i\beta}, \tag{13}$$

where μ is the wave propagation constant; α is the amplitude (real part) of the wave propagation constant λ; β is the phase (imaginary part) of the wave propagation constant. Similarly, the cases $\alpha = 0$ and $\alpha \neq 0$ corresponding to the cases $\lambda = 1$ and $\lambda \neq 1$ signify the pass bandgap and the stop bandgap, respectively. When using the exponential form, it is easier to determine the wave attenuation band if the amplitude (real part) of the wave propagation constant is larger than 0. The stop bandgap of the isolator could be determined based on the positive value of the real part of the wave propagation constant.

2.3　Dynamic model

Figure 4a shows the dynamic motion analysis diagram of the flexible plate supported vibration isolation system. Figure
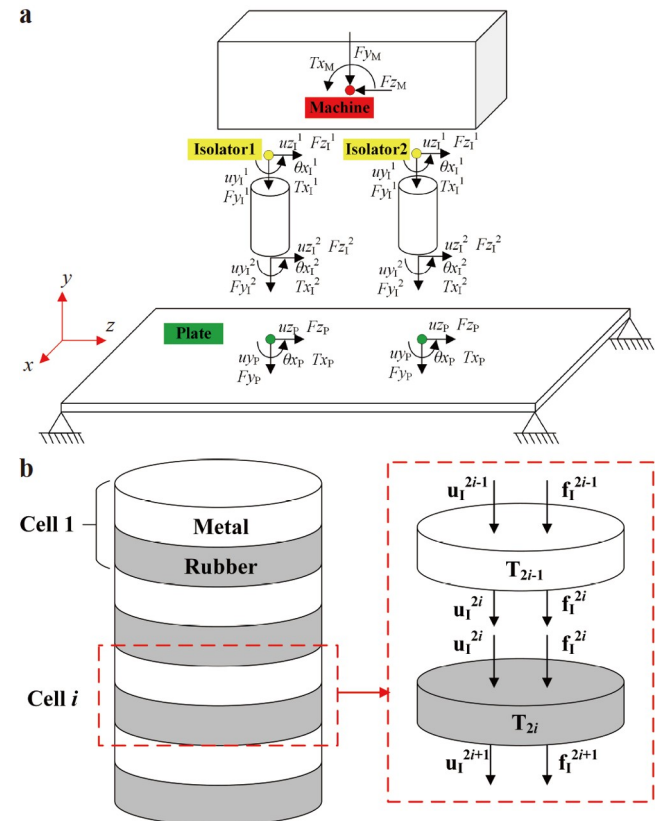

Figure 4　Motion analysis for **a** vibration isolation system and **b** isolator cell.

4b illuminates the dynamic motion analysis of the isolator cell. The dynamic model in this study is set up through the muti-subsystem method in which the flexible plate supported vibration isolation system divides into three main substructures: the rigid machine, the isolator mounts, and the supporting flexible plate. The three individual substructures are modeled in the form of the mobility or impedance matrix and are connected with others through the state variables of junction points. In the muti-subsystem method, the force and velocity of different substructures are transferred at the junctions. The machine is the vibration source which established as a rigid mass component. The continuous isolator mount is modeled as an elastic rod component. The periodic isolator mount and aperiodic isolator mount are modeled as elastic rod components combined in series. The plate is the flexible supported structure considering the elasticity effect. For ease of the dynamic isolation system analysis, only the plane motion of the mass, isolators, and the plate in the *x*-*z* plane are considered. The number of isolators is two.

In Fig. 4a, the velocity and force vectors of the machine $\mathbf{v}_M$ and $\mathbf{f}_M$, the plate $\mathbf{v}_P$ and $\mathbf{f}_P$, and the two isolator mounts $\mathbf{v}_I$ and $\mathbf{f}_I$ are respectively written as

$$\mathbf{v}_M = [vy_M, vz_M, \omega x_M]^T,$$
$$\mathbf{f}_M = [Fy_M, Fz_M, Tx_M]^T, \tag{14}$$

and

$$\mathbf{v}_P = [vy_P, vz_P, \omega x_P]^T,$$
$$\mathbf{f}_P = [Fy_P, Fz_P, Tx_P]^T, \tag{15}$$

and

$$\mathbf{v}_I = \left[vy_I^1, vz_I^1, \omega x_I^1, vy_I^2, vz_I^2, \omega x_I^2\right]^T,$$
$$\mathbf{f}_I = \left[Fy_I^1, Fz_I^1, Tx_I^1, Fy_I^2, Fz_I^2, Tx_I^2\right]^T, \tag{16}$$

where vy and vz are the linear velocities with respect to y- and z- axes; ωx is the linear angular velocity around the direction of x-axis; Fy and Fz are the linear forces in the direction of y- and z- axes; Tx is the angular moment around the x-axis; the subscripts M, P, and I denote the machine, plate, and isolator, respectively; the superscripts 1 and 2 denote the two different isolators, respectively.

The relations of the velocity and force vectors of the machine and the plate are associated through the dynamic mobility matrix of the rigid mass and flexible plate, which could be expressed as

$$\mathbf{v}_M = \mathbf{M}_M \mathbf{f}_M, \quad \mathbf{v}_P = \mathbf{M}_P \mathbf{f}_P, \tag{17}$$

where $\mathbf{M}_M$ and $\mathbf{M}_P$ are the mobility matrixes of the rigid mass and the flexible plate, respectively. Then, $\mathbf{M}_M$ is shown as

$$\mathbf{M}_M = \mathbf{V}_M \mathbf{H}^{-1} \mathbf{F}_M, \tag{18}$$

where

$$\mathbf{V}_M = \begin{bmatrix} 1 & 0 & 0 \\ 0 & 1 & (l_1 - \phi_e)/2 \\ 0 & 0 & 1 \\ 1 & 0 & 0 \\ 0 & 1 & -(l_1 - \phi_e)/2 \\ 0 & 0 & 1 \end{bmatrix},$$

$$\mathbf{H} = \begin{bmatrix} j\omega m & 0 & 0 \\ 0 & j\omega m & 0 \\ 0 & 0 & j\omega I \end{bmatrix},$$

$$\mathbf{F}_M = \begin{bmatrix} 1 & 0 & 0 & 1 & 0 & 0 \\ 0 & 1 & 0 & 0 & 1 & 0 \\ l_2/2 & (l_1 - \phi_e)/2 & 1 & l_2/2 & -(l_1 - \phi_e)/2 & 1 \end{bmatrix}.$$

In the matrix of $\mathbf{V}_M$, $\mathbf{H}$, and $\mathbf{F}_M$, l_1 and l_2 are the dimensions of the rigid machine; ϕ_e is the diameter of the isolator; m is mass; I is the moment of inertia about the x-axis; ω is the angular frequency; and j is the imaginary unit.

The dynamic motion of the isolator mounting could be expressed with an impedance matrix in the form of

$$\mathbf{f}_I = \mathbf{Z}_I \mathbf{v}_I, \tag{19}$$

where $\mathbf{Z}_I$ is the impedance matrix of the isolator mounting, which is represented as ref. [28]

$$\mathbf{Z}_I = \begin{bmatrix} \mathbf{Z}_I^{(1,1)} & \mathbf{Z}_I^{(1,2)} \\ \mathbf{Z}_I^{(2,1)} & \mathbf{Z}_I^{(2,2)} \end{bmatrix}$$

$$= \begin{bmatrix} Z_{uy^1 Fy^1} & 0 & Z_{uy^1 Tx^1} & Z_{uy^1 Fy^2} & 0 & Z_{uy^1 Tx^2} \\ 0 & Z_{uz^1 Fz^1} & 0 & 0 & Z_{uz^1 Fz^2} & 0 \\ Z_{\theta x^1 Fy^1} & 0 & Z_{\theta x^1 Tx^1} & Z_{\theta x^1 Fy^2} & 0 & Z_{\theta x^1 Tx^2} \\ Z_{uy^2 Fy^1} & 0 & Z_{uy^2 Tx^1} & Z_{uy^2 Fy^2} & 0 & Z_{uy^2 Tx^2} \\ 0 & Z_{uz^2 Fz^1} & 0 & 0 & Z_{uz^2 Fz^2} & 0 \\ Z_{\theta x^2 Fy^1} & 0 & Z_{\theta x^2 Tx^1} & Z_{\theta x^2 Fy^2} & 0 & Z_{\theta x^2 Tx^2} \end{bmatrix}, \tag{20}$$

where the elements in the impedance matrix $\mathbf{Z}_I$ are expressed in Appendix A.

The transfer matrix of the beam isolator can be obtained by inversion processing of the mobility matrix of the beam isolator

$$\mathbf{T}_I =$$
$$\begin{bmatrix} \mathbf{Z}_I^{(1,1)}\left(\mathbf{Z}_I^{(2,1)}\right)^{-1} & \mathbf{Z}_I^{(1,2)} - \mathbf{Z}_I^{(1,1)}\left(\mathbf{Z}_I^{(2,1)}\right)^{-1}\mathbf{Z}_I^{(2,2)} \\ \left(\mathbf{Z}_I^{(2,1)}\right)^{-1} & -\left(\mathbf{Z}_I^{(2,1)}\right)^{-1}\mathbf{Z}_I^{(2,2)} \end{bmatrix}. \tag{21}$$

In Fig. 4b, the *N* number aperiodic isolator rods are combined together in series. The aperiodic isolator cells and periodic isolator cells are transferred through the force and velocity vectors $\mathbf{v}_I^i$ and $\mathbf{f}_I^i$. The transfer matrix of the aperiodic isolator is calculated by multiplying the multi isolator cells

$$\mathbf{T}_I = \mathbf{T}_1 \mathbf{T}_2 \cdots \mathbf{T}_N = \begin{bmatrix} \mathbf{T}_I^{(1,1)} & \mathbf{T}_I^{(1,2)} \\ \mathbf{T}_I^{(2,1)} & \mathbf{T}_I^{(2,2)} \end{bmatrix}. \tag{22}$$

Through mathematical calculation, the impedance form of the aperiodic isolator is shown as follows:

$$\mathbf{Z}_I =$$
$$\begin{bmatrix} \mathbf{T}_I^{(1,1)}\left(\mathbf{T}_I^{(2,1)}\right)^{-1} & \mathbf{T}_I^{(1,2)} - \mathbf{T}_I^{(1,1)}\left(\mathbf{T}_I^{(2,1)}\right)^{-1}\mathbf{T}_I^{(2,2)} \\ \left(\mathbf{T}_I^{(2,1)}\right)^{-1} & -\left(\mathbf{T}_I^{(2,1)}\right)^{-1}\mathbf{T}_I^{(2,2)} \end{bmatrix}. \tag{23}$$

The dynamic motions of the machine and plate can be grouped together in the form of

$$\mathbf{v}_{MP} = \mathbf{M}_{MP}\mathbf{f}_{MP}, \tag{24}$$

where the mobility matrix $\mathbf{M}_{MP}$, force vector $\mathbf{f}_{MP}$, and velocity vector $\mathbf{v}_{MP}$ of the group subsystems are given as

$$\mathbf{M}_{MP} = \begin{bmatrix} \mathbf{M}_M & \mathbf{0} \\ \mathbf{0} & \mathbf{M}_P \end{bmatrix}, \quad \mathbf{u}_{MP} = \begin{Bmatrix} \mathbf{v}_M \\ \mathbf{v}_P \end{Bmatrix},$$
$$\mathbf{f}_{MP} = \begin{Bmatrix} \mathbf{f}_M \\ \mathbf{f}_P \end{Bmatrix}, \tag{25}$$

where $\mathbf{M}_M$ and $\mathbf{M}_P$ are mobility matrices of the machine and plate, respectively; $\mathbf{v}_M$, $\mathbf{v}_P$, $\mathbf{f}_M$, and $\mathbf{f}_P$ are given in Eqs. (14) and (15). The mobility matrix of the plate $\mathbf{M}_P$ is shown as [28]

$$\mathbf{M}_P =$$
$$\begin{bmatrix} m_{uyFy}^{11} & 0 & 0 & m_{uyFy}^{12} & 0 & 0 \\ 0 & m_{uzFz}^{11} & m_{uzTx}^{11} & 0 & m_{uzFz}^{12} & m_{uzTx}^{12} \\ 0 & m_{\theta xFz}^{11} & m_{\theta xTx}^{11} & 0 & m_{\theta xFz}^{12} & m_{\theta xTx}^{12} \\ m_{uyFy}^{21} & 0 & 0 & m_{uyFy}^{22} & 0 & 0 \\ 0 & m_{uzFz}^{21} & m_{uzTx}^{21} & 0 & m_{uzFz}^{22} & m_{uzTx}^{22} \\ 0 & m_{\theta xFz}^{21} & m_{\theta xTx}^{21} & 0 & m_{\theta xFz}^{22} & m_{\theta xTx}^{22} \end{bmatrix}, \tag{26}$$

where the elements in the mobility matrix $\mathbf{M}_P$ are expressed in Appendix B.

The relations of $\mathbf{v}_{MP}$, $\mathbf{f}_{MP}$, and the excitation force $\mathbf{q}_{MP}$ can be obtained by

$$\mathbf{u}_{MP} = (\mathbf{I} + \mathbf{M}_{MP}\mathbf{Z}_I)\mathbf{M}'_{MP}\mathbf{q}_{MP}, \tag{27}$$

$$\mathbf{f}_{MP} = -\mathbf{Z}_I(\mathbf{I} + \mathbf{M}_{MP}\mathbf{Z}_I)\mathbf{M}'_{MP}\mathbf{q}_{MP}, \tag{28}$$

and the form of the excitation force, which only applied on the machine, is written as

$$\mathbf{q}_{MP} = [Fy_M, Fz_M, Tx_M, 0, 0, 0]^T. \tag{29}$$

In Eqs. (27) and (28), $\mathbf{M}_{MP}$ is given as

$$\mathbf{M}'_{MP} = \begin{bmatrix} \mathbf{M}' & \mathbf{0} \\ \mathbf{0} & \mathbf{0} \end{bmatrix}, \tag{30}$$

where $\mathbf{M}' = -\mathbf{V}_M\mathbf{H}^{-1}\mathbf{L}$ and $\mathbf{L} = \begin{bmatrix} -1 & 0 & 0 \\ 0 & -1 & 0 \\ 0 & 0 & -1 \end{bmatrix}$.

The $\mathbf{v}_{MP}$ and $\mathbf{f}_{MP}$ are associated with $\mathbf{v}_I$ and $\mathbf{f}_I$ according to the continuity principle

$$\mathbf{v}_I = \mathbf{v}_{MP}, \tag{31}$$

and equilibrium principle

$$\mathbf{f}_I = -\mathbf{f}_{MP}. \tag{32}$$

The total input power due to the excitation of the machine is given by

$$P_t = 10\log_{10}\left[\frac{1}{2}Re\left(\mathbf{f}_M^H\mathbf{v}_M\right)/P_{ref}\right], \tag{33}$$

and the power transmitting to the junction point of the plate is given by

$$P_r = 10\log_{10}\left[\frac{1}{2}Re\left(\mathbf{f}_P^H\mathbf{v}_P\right)/P_{ref}\right], \tag{34}$$

where the reference power is $P_{ref} = 10^{-12}$ W.

The vertical mean square velocity level is defined as

$$Lv = 10\log_{10}\left(vz^2/vz_0^2\right), \tag{35}$$

where the reference velocity is $vz_0 = 10^{-9}$ m/s.

3. Optimization

Based on the Eqs. (5)-(8) in Sect. 2.2, the vibration attenuation bandgap of the isolator mainly depends on the amplitude of the wave propagation constant α. According to Eq. (5), the longitudinal length L, material Young's modulus E, and material density ρ are three parameters that could adjust the stop bandgap of the aperiodic isolator. In the optimization problem of this study, the longitudinal length L is selected as the main design parameter as other parameters are difficult to vary in general engineering applications. The objective of the optimization is to find the optimal longitudinal lengths of the aperiodic isolator for suppressing the internal resonances. The PSO optimization algorithm and the flow chart of the optimization progress are clearly discussed in this section.

3.1 PSO optimization algorithm

The PSO algorithm is firstly proposed by Kennedy and Eberhart. Compared to other iterative optimization algorithms such as genetic algorithm, the PSO algorithm has the advantage that only follows the optimal particle during the search iteration process. Therefore, the information exchanged between feasible solutions is relatively simple, resulting to converge easily and quickly. The PSO algorithm could avoid problems such as parameter adjustment, con-

straint condition setting, and iteration convergence difficulty.

According to the PSO algorithm, a particles' group within the feasible solution space is randomly initialized. Each particle represents a potential optimal solution to the optimization problem. The characteristics of the particles are represented by their position x_i, velocity v_i, and fitness value p_i. The fitness value is determined by the fitness function of the optimization problem. The searching process of the PSO algorithm is given as

$$v_i^{k+1} = wv_i^k + C_1 * \text{rand}_1\left(p_i^k - x_i^k\right) + C_2 * \text{rand}_2\left(p_g^k - x_i^k\right), \tag{36}$$

$$x_i^{k+1} = x_i^k + v_i^{k+1}, \tag{37}$$

$$w = w_1 - (w_1 - w_2)\frac{\text{iter}}{\text{Max iter}}, \tag{38}$$

where superscripts $k + 1$ and k denote parameters at k and $k +1$ iterations, respectively; p_g^k is the global best position in the particle group; rand_1 and rand_2 are stochastic values within [0,1]. The value w determines the searching areas size of particles. The searching areas size of w is changing from w_1 to w_2 according to Eq. (38). In the PSO algorithm, we hope the searching areas size is getting smaller during iterations. The iter is the current iteration number and Max_iter is the max iteration number. In this study, $C_1 = 0.5$, $C_2 = 0.5$, $w_1 = 0.8$, and $w_2 = 0.2$.

3.2 Length optimization design of the aperiodic isolator

As the aperiodic isolator has four cells, the optimization variables are the position of particles in the vector form of $\mathbf{x}_i$ $= [x_1, x_2, x_3, x_4, x_5, x_6, x_7, x_8]^{\text{T}}$, where each particle's position represents the length of the aperiodic isolator cell. The total length of the metal or rubber component of the aperiodic isolator are set as 80 mm. The lengths of the metal rod and the rubber rod are within [5, 25] mm. The optimization variables are shown in Fig. 5. According to the wave propagation theory in Sect. 2.2, the internal resonances are
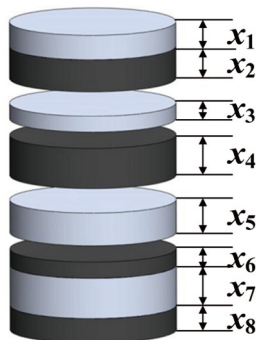

Figure 5 Length optimization parameters of the aperiodic isolator.

decreased with the increase of the real part of wave propagation constant α. The widest stop bandgap is achieved by decreasing the occurrence times that the real part of wave propagation constant α is smaller than a given positive constant. Hence, the fitness function is the minimum occurrence times of α smaller than a constant value in the target frequency band, which is given as

$$F_{\text{obj}} = \min \sum_{f \in (f_1, f_2)} A, \tag{39}$$

$$\begin{cases} A = 1, \text{ if } \alpha(f) < C_0, f \in \left(f_1, f_1'\right), \\ A = 0, \text{ if } \alpha(f) > C_0, f \in \left(f_1', f_2\right), \end{cases} \tag{40}$$

where f_1-f_2 is the target frequency band, and C_0 is the positive constant. This fitness function is established to try to obtain an optimized transfer constant curve that amplitude above C_0 in the frequency band f_1-f_2, which realizes the internal resonances attenuation. Figure 6 shows the flow chart of the proposed optimization algorithm based on the PSO method.

4. Results

In this section, numerical investigations are carried out including the numerical model verification, vibration isolation performances comparison of the isolators, internal resonances suppression by the aperiodicity and damping, and parameter optimization of the aperiodic isolator through optimization method. An experiment of the vibration isolation systems is conducted. The above dynamic analyses
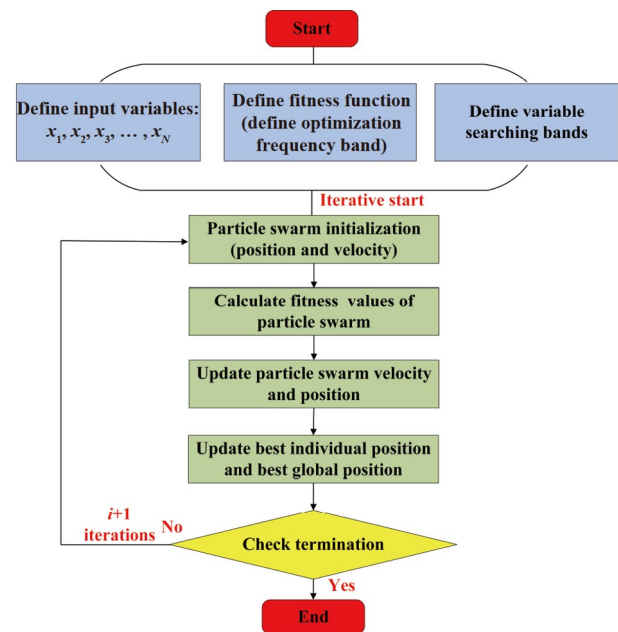

Figure 6 A flow chart of the optimization design for the aperiodic isolator.

Y. Liu, *et al. Acta Mech. Sin.*, Vol. 41, 523535 (2025)

523535-8

focus on the dynamic characteristics of vibration isolation systems within 1-5000 Hz.

4.1   Dynamic model verification with FEM method

For validating the reliability of the numerical method proposed for the vibration isolation system, the finite element models of the continuous isolator, periodic isolator and aperiodic isolator are established with the same numerical model parameters. The machine is a rigid mass with dimensions of 0.52 m × 0.3 m × 0.25 m. Its mass and moment of inertia are 105.3 kg and 3.16 kg m^2, respectively. The dimensions of the supporting plate are 1 m × 1.5 m × 0.01 m. The material of the plate is aluminum. Its Young's modulus is 71 GPa. Its Poisson's ratio is 0.33. Its loss factor is 0.005. The diameters of the three isolators are 0.1 m. The continuous isolator has a 0.08 m height. The periodic isolator and aperiodic isolator have four sets of isolator cells. Table 1 shows the dimensions of the periodic isolator and aperiodic isolator. x is the length of the isolator cell. For the rubber material, its Young's modulus is 1 MPa, and its Poisson's ratio is 0.49. For the metal material, its metal property is the same as the plate. Figure 7 shows the diagram of the finite element model. The machine is set as a rigid body. The isolator is established as a beam element. The plate is modeled as an elastic element. The excitation force is considered in the vertical direction. The flexible plate is simply supported. The calculation frequency range is 1-5000 Hz. The vertical mean square velocity level at the isolator foot obtained by the numerical method and the finite element method are compared in Fig. 8. The vertical mean square velocity level of the continuous isolator, periodic isolator, and aperiodic isolator using the numerical method are similar with that obtained from the FEM, which proves the reliability of the numerical method in this study.

Table 1   Dimensions of the periodic isolator and aperiodic isolator.

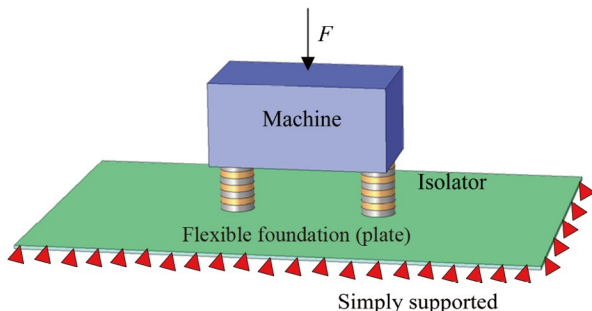| Lengths	x_1, x_2	x_3, x_4	x_5, x_6	x_7, x_8
Periodic isolator (mm)	20	20mm	20	20
Aperiodic isolator (mm)	14mm	18	22	26

Figure 7   FEM model of the vibration isolation system.

4.2   Comparison of the vibration isolation systems

Figure 9 compares the total input power and total power flow transfer into the plate of the three different vibration isolation systems with continuous isolator, periodic vibration isolator and aperiodic isolator, respectively. P_t is de-
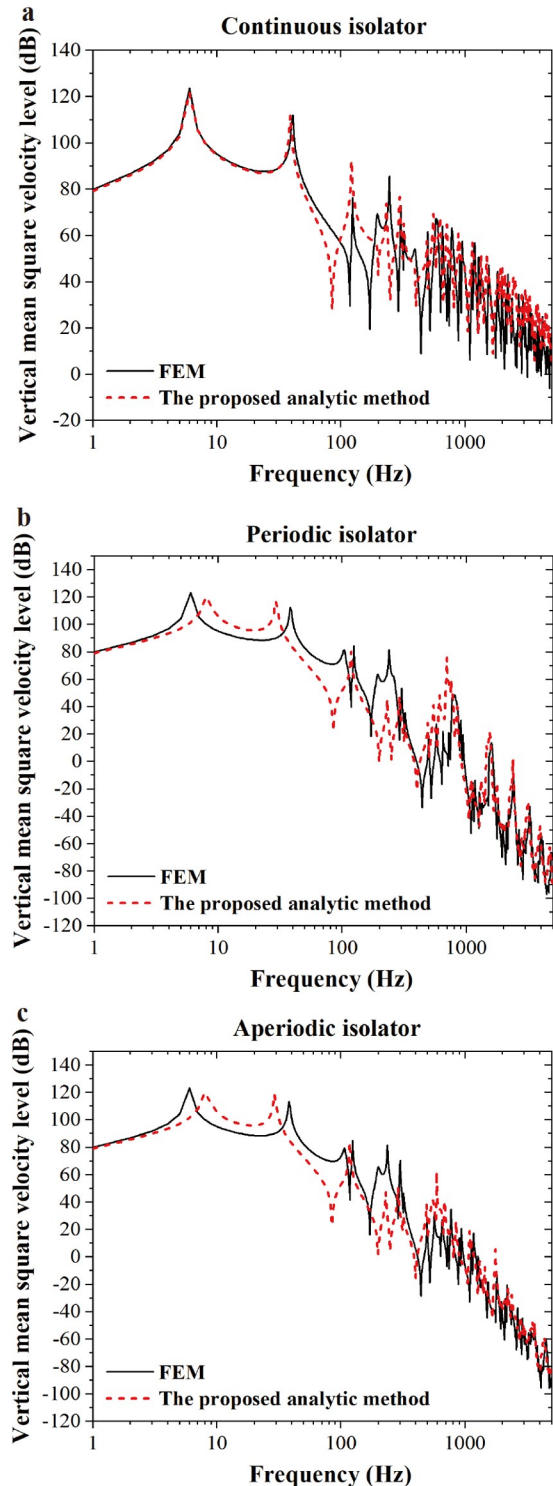

Figure 8   Vertical mean square velocity level at the junction of the plate of **a** continuous isolator, **b** periodic isolator, and **c** aperiodic isolator.

fined as the total input power from the machine and P_r is defined as the power transmitting to the flexible plate foundation. In these cases, the loss factor ξ of the rubber material is defined as 0.05. The loss factor ξ of the metal material is 0.005. P_r of the continuous vibration isolation system is 15 dB lower than P_t in the frequency band
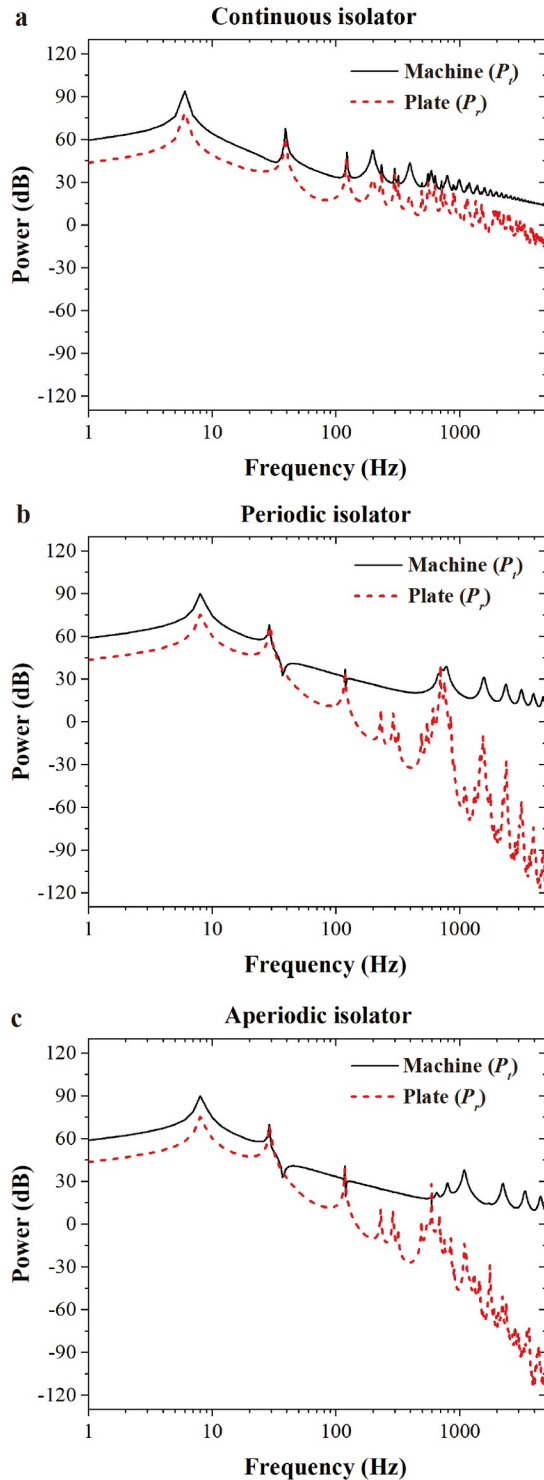

(150-5000Hz) as shown in Fig. 9a. In Fig. 9b and c, P_r of the periodic vibration isolation system and the aperiodic vibration isolation system show significant vibration isolation performance, being 40-100 dB lower than P_t in the frequency band (150-5000 Hz). In the aperiodic isolation, more modal peaks of P_r are observed in the high frequency band. The high frequency modal peaks of P_r of the aperiodic vibration isolation system attenuate more obviously than those of the periodic vibration isolation system. Hence, the aperiodic vibration isolation system could degrade the internal resonances of the isolator.

Real part of transfer constant is calculated through the wave transmission analysis of the isolator, which represents the wave attenuation performance. Figure 10 shows the double Y-curves of the isolator in the periodic vibration isolation system, which the solid-line curve and the dash-line curve represent the power and the real part of the transfer constant, respectively. The symbols "○" in the dash-line annotate the sudden attenuation drop in frequency bands, which are generated from the internal resonances of the isolator. The internal resonances are changed with the geometrical and material parameters of the isolator. The symbols "◊" in the solid-line corresponding represent the internal resonances. The other peaks are caused by the flexible plate. Figure 10 illustrates that internal resonances are evident in the periodic isolator, which generates large vibration peaks in middle and high frequencies. According to Fig. 9c, the aperiodic isolator could overcome this problem.

4.3 The internal resonances suppression by the aperiodicity and damping

Aperiodic isolator has aperiodicity characteristics compared with periodic isolator. The damping of the isolator could attenuate the high frequency vibration due to its viscoelastic
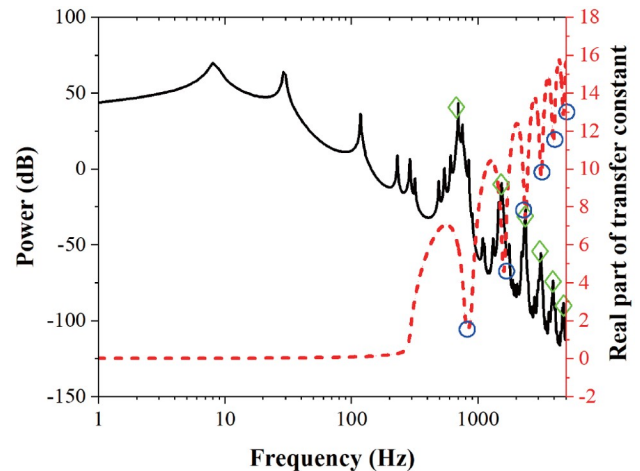
Figure 9 Comparison of total input power from the machine and the power transmitting to the plate of the vibration isolation system with **a** continuous isolator, **b** periodic isolator, and **c** aperiodic isolator.

Figure 10 Vibration peaks caused by the internal resonances in the periodic isolator.

property. Figure 11a-c compares the continuous isolator, periodic isolator and aperiodic isolator under the same damping, which proves the aperiodicity influence on the internal resonances control. In Fig. 11a-c, the effect of the aperiodicity on the control of the internal resonances is apparent when the damping is small, and the effect of the

aperiodicity on the control of the internal resonances is small when the damping is large. In Fig. 11a, the number of the internal resonances of the aperiodic isolator is increased and the internal resonances are effectively controlled compared with the periodic isolator, which confirmed the conjecture in the first paragraph in Sect. 2.2. Figure 11d-f
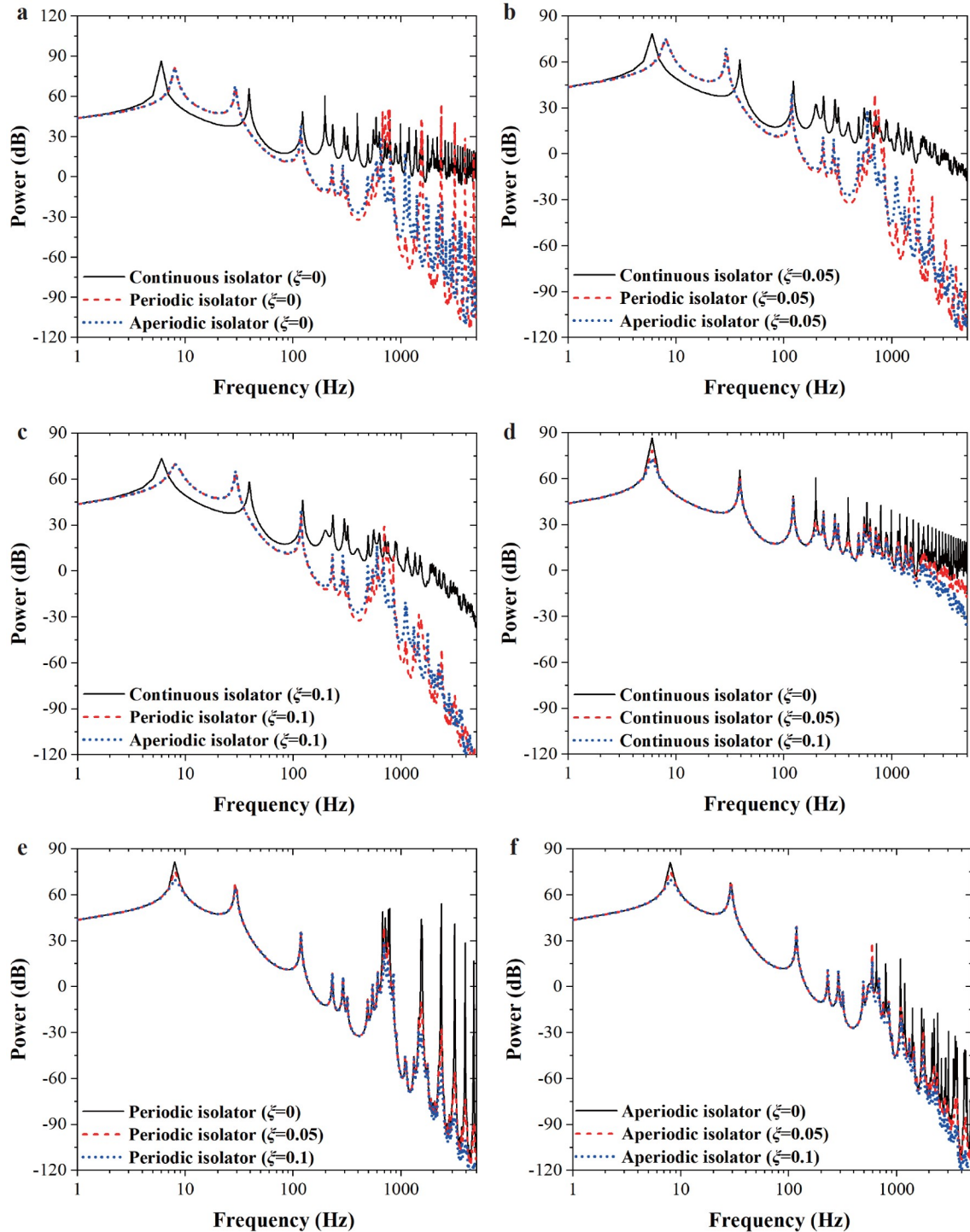

Figure 11 Power of the plate junction of the vibration isolation systems. **a** different isolators considering damping of isolator $\xi=0$, **b** different isolators considering damping of isolator $\xi=0.05$, **c** different isolators considering damping of isolator $\xi=0.1$, **d** continuous isolator with different damping, **e** periodic isolator with different dampings, and **f** aperiodic isolator with different damping.

compares the vibration isolation systems with different damping ξ of 0, 0.05, and 0.1, which prove the damping influence on the internal resonances control. From Fig. 11d-f, it could be seen that the high frequency modal peaks of the vibration isolation system considering the damping of the isolator (ξ=0.05 and ξ=0.1) fail more distinctly than those without damping of the isolator (ξ=0). It demonstrates that the damping of the isolator effectively degrades the vibration peaks including internal resonances.

Figure 12 shows the first four orders of internal resonances reduction effect by the aperiodicity and the damping of the isolator. In Fig. 12a, the comparison of the periodic isolator and aperiodic isolator signifies that the internal resonances reduction effect of the aperiodic isolator is significantly visible in the case of small damping $\xi = 0$; the internal resonances reduction effect of the aperiodic isolator is poor in the case of large damping $\xi = 1$ with no internal resonances reduction at modes 2 and 4. In Fig. 12b, the comparison of the isolators with damping and without damping suggests that the internal resonances reduction is increased with the mode under the same damping; the internal resonances reduction is increased with damping under the same mode.

4.4 The wave propagation characteristic in periodic and aperiodic isolators

According to Sect. 2.2, the wave attenuation performance is associated with the real part of the transfer constant. The wave attenuates more as the real part of the transfer constant gets larger. Figure 13a-c shows the wave attenuation performance comparison of the periodic isolator and aperiodic isolator under the same damping. In Fig. 13a, the periodic isolator has periodic distributed stop band gaps, and the aperiodic isolator has nonuniform distributed stop band gaps. The internal resonances show periodically in the

periodic isolator without damping. As the aperiodic isolator, without damping opens stop bandgaps at middle and high frequencies, the internal resonances are effectively degraded. In Fig. 13b and c, the wave attenuation performance of the aperiodic isolator considered the damping behaves better than that of the periodic isolator as it avoids some large valleys in the whole frequency band. Figure 13d and e show the wave attenuation performance comparison of the same isolator with different damping. In Fig. 13d and e, damping makes the valleys in the real part of transfer constant curve raise in both periodic isolator and aperiodic isolator. The damping of the isolator improves the wave attenuation performance in middle and high frequencies, for both periodic isolator and aperiodic isolator. Hence, the internal resonances of the isolator could be significantly controlled by the aperiodicity and the damping of the isolator.

4.5 Optimization of the aperiodic isolator

In the optimized design of the aperiodic isolator, the length parameters of the metal rod and rubber rod are set as design parameters. The optimization method of the aperiodic isolator is introduced in Sect. 3.2. In this section, three different optimization cases are selected for verifying the effective of the optimized method. The target frequency band and the fitness function of the cases are shown in Table 2. The first optimization case is to reduce the maximum modal peak in the frequency band of 300-1000 Hz. The aim of the second optimization case is minimizing the modal peak around 1000-2000 Hz. The aim of the last optimization case is decreasing the modal peak in 300-2000 Hz. The fitness functions are determined according to the different objectives, which are given in Table 2.

Figure 14 shows the comparison of the power response of the three optimization cases. Figure 14a shows the P_r of the optimized aperiodic isolator has 28 dB modal peak reduc-
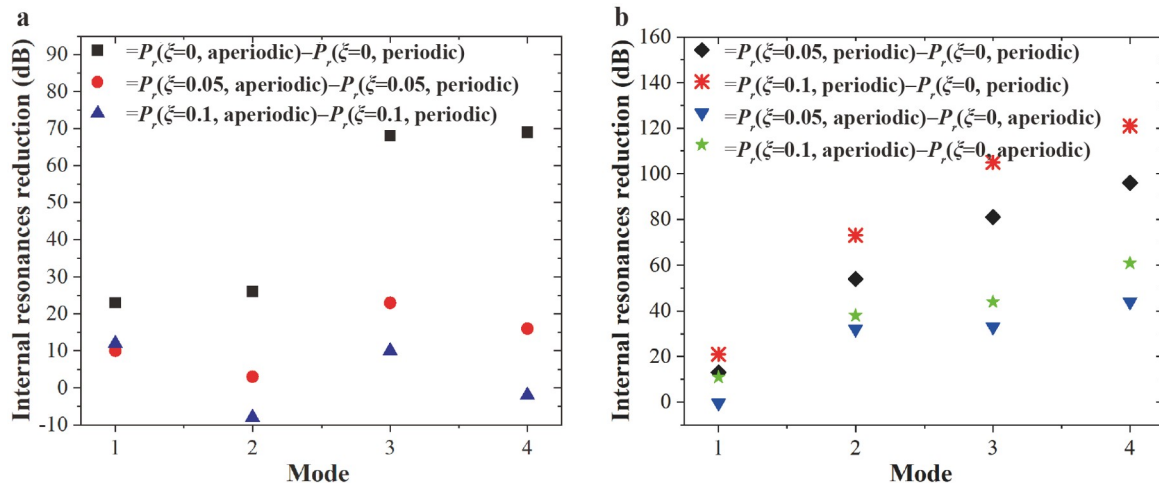

Figure 12 Internal resonances control effect by **a** the aperiodicity and **b** the damping of the isolator.

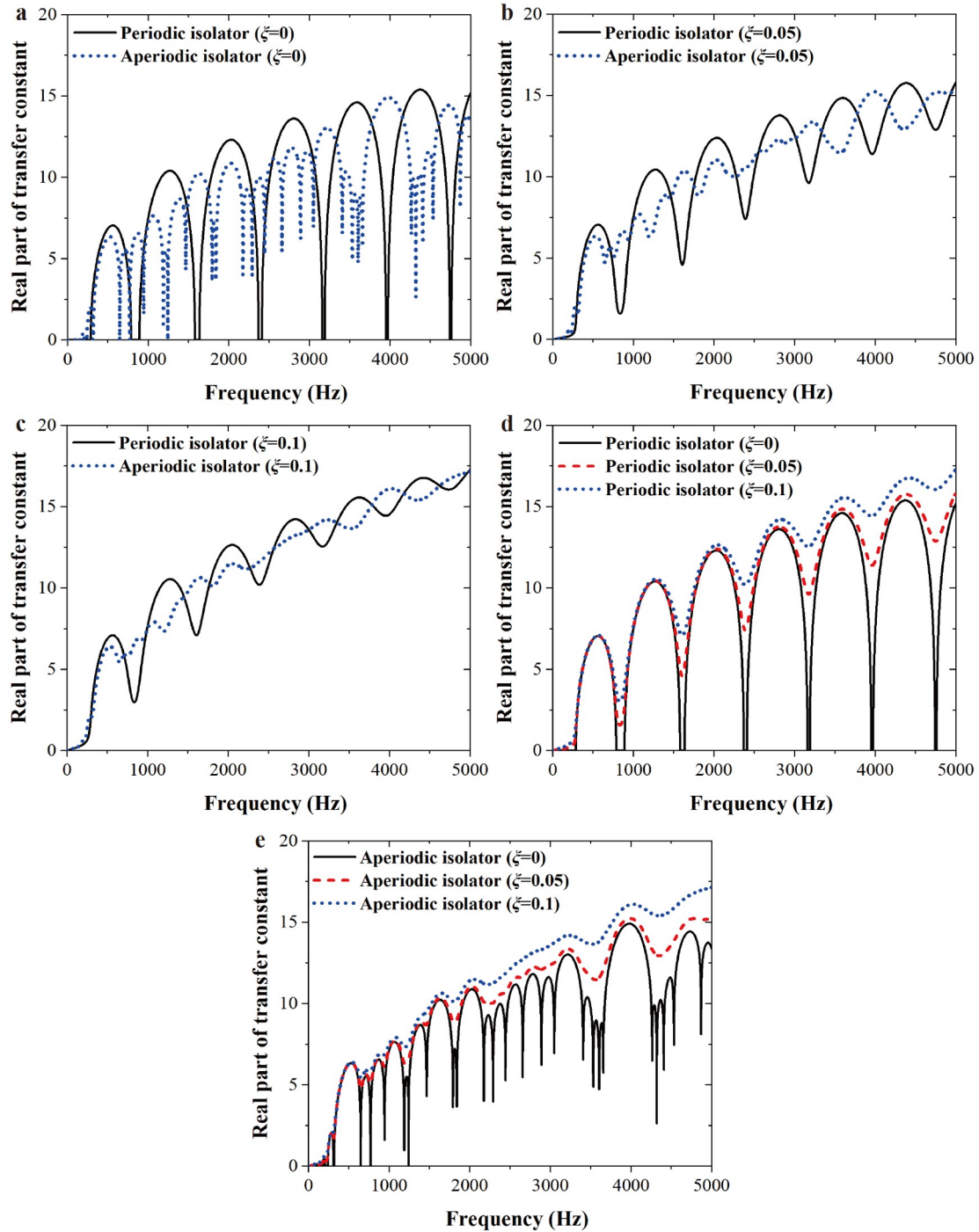Y. Liu, *et al. Acta Mech. Sin.*, Vol. 41, 523535 (2025)

523535-12

Figure 13 Real part of transfer constant of **a** periodic and aperiodic isolators considering damping of isolator $\xi = 0$, **b** periodic and aperiodic isolators considering of isolator $\xi = 0.05$, **c** periodic and aperiodic isolators considering damping of isolator $\xi = 0.1$, **d** periodic isolator with different material damping, and **e** aperiodic isolator with different material damping.

tion in the frequency band 300-1000 Hz compared to that without optimized design. Figure 14b displays the modal peak of P_r of the optimized aperiodic isolator could reduce 11 dB in the frequency band 1000-2000 Hz. Figure 14c shows the modal peak of P_r of the optimized aperiodic isolator drop 33 dB in the frequency band 300-1000 Hz and 14 dB in the frequency band 1000-2000 Hz, respectively.

Table 3 summarizes the optimized results of the three different cases, giving the optimal length dimensions of the three aperiodic isolators and their corresponding optimized effect. Table 3 illustrates that the modal peak reduction in the objective frequency band could be achieved by a simply length parameter adjustment of the aperiodic isolator using the proposed optimization method.

Table 2 The objective frequency and fitness function of the cases

| Case	Target frequency (Hz)	Fitness function
1	300-1000	$F_{obj} = \min\sum_{f} A,\ f \in (300\ \text{Hz}, 5000\ \text{Hz}),$ $\begin{cases} A = 1,\ \text{if}\ \alpha(f) < 6,\ f \in (300\ \text{Hz},\ 1000\ \text{Hz}), \\ A = 0,\ \text{if}\ \alpha(f) > 6,\ f \in (300\ \text{Hz},\ 1000\ \text{Hz}), \\ A = 0,\ f \in (1001\ \text{Hz},\ 5000\ \text{Hz}) \end{cases}$
2	1000-2000	$F_{obj} = \min\sum_{f} A,\ f \in (300\ \text{Hz},\ 5000\ \text{Hz}),$ $\begin{cases} A = 1,\ \text{if}\ \alpha(f) < 8,\ f \in (1000\ \text{Hz},\ 2000\ \text{Hz}), \\ A = 0,\ \text{if}\ \alpha(f) > 8,\ f \in (1000\ \text{Hz},\ 2000\ \text{Hz}), \\ A = 0,\ f \in (300\ \text{Hz}, 999\ \text{Hz}),\ (2001\ \text{Hz},\ 5000\ \text{Hz}) \end{cases}$
3	300-2000	$F_{obj} = \min\sum_{f} A,\ f \in (300\ \text{Hz},\ 5000\ \text{Hz}),$ $\begin{cases} A = 1,\ \text{if}\ \alpha(f) < 6,\ f \in (300\ \text{Hz},\ 1000\ \text{Hz}), \\ A = 0,\ \text{if}\ \alpha(f) > 6,\ f \in (300\ \text{Hz},\ 1000\ \text{Hz}), \\ A = 1,\ \text{if}\ \alpha(f) < 8,\ f \in (1001\ \text{Hz},\ 2000\ \text{Hz}), \\ A = 0,\ \text{if}\ \alpha(f) > 8,\ f \in (1001\ \text{Hz},\ 2000\ \text{Hz}), \\ A = 0,\ f \in (2001\ \text{Hz},\ 5000\ \text{Hz}) \end{cases}$
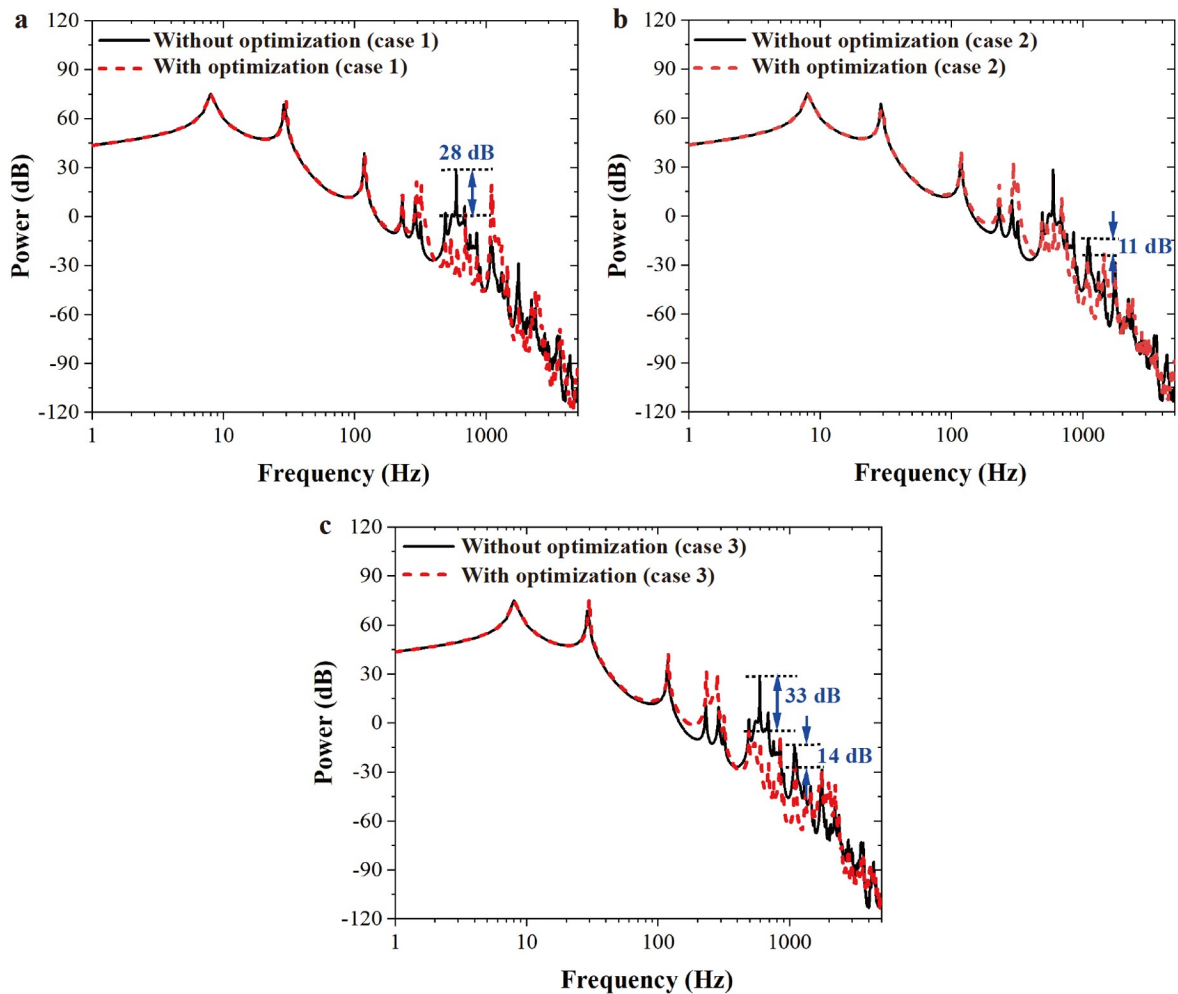
Figure 14 Optimization power response results of **a** case 1, **b** case 2, and **c** case 3.

Table 3   Optimization results of the cases

Case	Optimized dimensions	Optimization effect
1	$[x_1, x_2, x_3, x_4, x_5, x_6, x_7, x_8]$ $= [12, 21, 13, 18, 12, 20, 43, 21]$ mm	↓28 dB (300-1000 Hz)
2	$[x_1, x_2, x_3, x_4, x_5, x_6, x_7, x_8]$ $= [6, 16, 20, 20, 9, 15, 45, 29]$ mm	↓11 dB (1000-2000 Hz)
3	$[x_1, x_2, x_3, x_4, x_5, x_6, x_7, x_8]$ $= [7, 22, 9, 16, 8, 19, 56, 23]$ mm	↓33 dB (300-1000 Hz) ↓14 dB (1000-2000 Hz)

4.6   Experimental results

For verifying the vibration isolation performances of the continuous isolators, periodic isolator, and aperiodic isolator, vibration isolation experiments are taken. The layouts of the vibration isolation test platform are displayed in Fig. 15. The experimental configuration combines a test computer (software), data acquisition panel, impact hammer, two acceleration sensors, and vibration isolation models. The vibration isolation models are composed of the aluminum mass block of 16 kg, the aluminum plate with 0.8 m × 0.5 m × 0.005 m, and the isolators. Figure 15b shows the test samples of the three isolators. The material of the continuous isolator is rubber. The materials made of the periodic isolator and aperiodic isolator are aluminum and rubber. The three isolators are cylinder-shaped with 0.1 m diameter. The continuous isolator has a 0.08 m height. The dimensions of the periodic isolator and the aperiodic isolator are the same as in Table 1. The two acceleration sensors are respectively sticked to the upper panel and lower panel of the isolator. The acceleration transmission loss of the vibration isolation experiment is defined as the vibration acceleration level difference of the two acceleration sensors.

Figure 16 shows the experimental results of the acceleration transmission loss of the three different isolators. From Fig. 16, the acceleration transmission loss of the three different isolators is generally increased with the frequency. The acceleration transmission losses of the periodic isolator and the aperiodic isolator are greater than that of the continuous isolator. This experimental result proves that the periodic isolator and aperiodic isolator are effectively in stopping wave propagation above 500 Hz comparing to the continuous isolator. The difference between the periodic isolator and the aperiodic isolator is small according to the experimental results. According to the results discussion of Figs. 11 and 13, this may be due to the large damping of the isolator, which leads to the unobvious contrast between the two isolators.
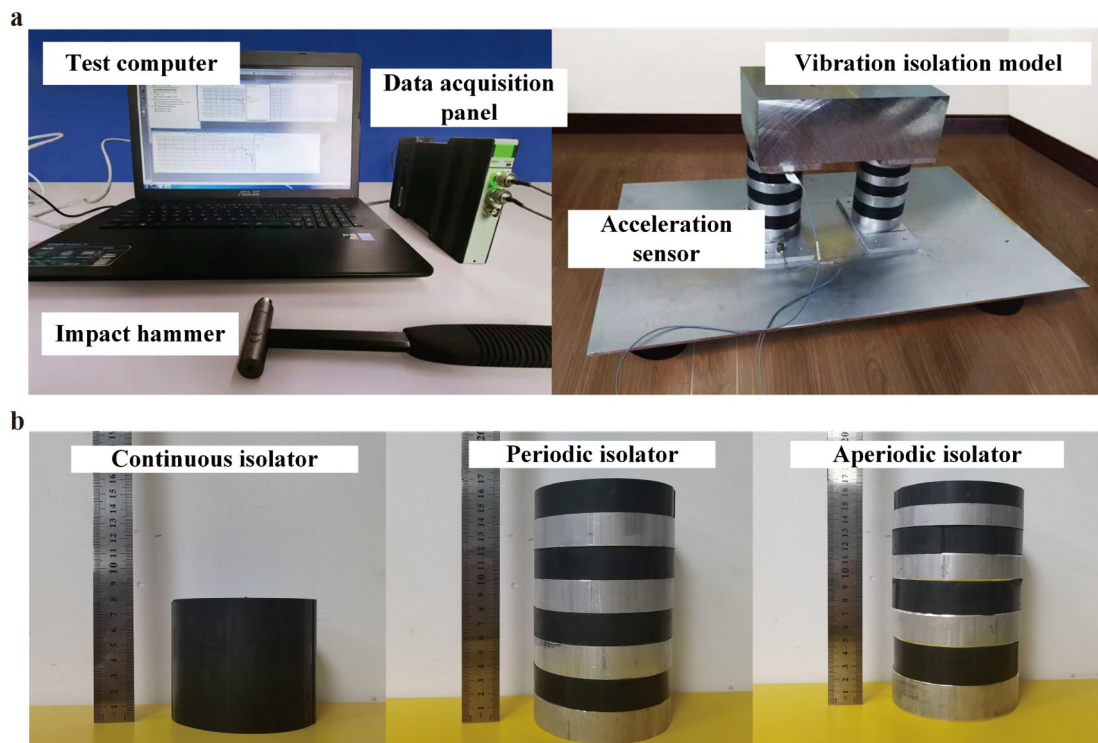

Figure 15   **a** Experimental configuration of the vibration isolation model and **b** test samples of the three isolators.
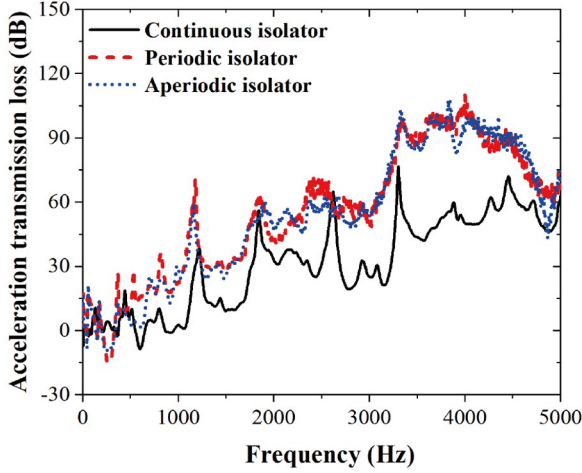
Figure 16 Acceleration transmission loss of the three different isolators in vibration isolation experiment.

5. Conclusions

In this study, the vibration isolation performances of the continuous isolator, periodic isolator, and aperiodic isolator have been studied. The internal resonance suppression mechanism of the aperiodic isolator is firstly proposed. Mutisubsystems method and transfer matrix method are utilized to analyze the dynamic characteristic of the vibration isolation system, which accuracy is proved by comparing with finite element analysis. The lengths of the aperiodic isolator are optimized based on the PSO method for enhancing the internal resonances reduction effect. The vibration isolation experimental results of the three isolators are discussed. As the rod element is considered in this model, the deformation in the lateral direction of the isolator is ignored, which causes stiffness deviation of the isolator [30]. The study would overcome this problem in future studies. The main conclusions are given as:

(1) The periodic isolator and aperiodic isolator extremely reduce the power transmitting to plate in the vibration isolation system in the middle and high frequencies than that of the continuous isolator. In the numerical cases of the study, the power of the plate foundation of the periodic isolator and the aperiodic isolator reduces 25-85 dB in the frequency band (150-5000Hz) comparing to that of the continuous isolator.

(2) The internal resonances of the isolator are generated due to the mass effect of the isolator. The mechanism of the internal resonances control of the aperiodic isolator is that it increases the standing wave types and degrades the internal resonances energy in the frequency spectrum. The internal resonances control effect of the aperiodic isolator works well when the damping of the isolator is small, and is not visible when the damping of the isolator is large. The internal resonance reduction due to the damping of the isolator is increased with modal order.

(3) The length optimization method of the aperiodic isolator is effective for internal resonances control. The optimized method is available to improve the vibration peaks control of the isolation system with the aperiodic isolator. In the case study, the vibration peaks achieve 33 dB in the target frequency band of 300-1000 Hz and 14 dB in the target frequency band of 1000-2000 Hz.

(4) The experimental results verify that the vibration attenuation effects of the periodic isolator and the aperiodic isolator in middle and high frequency are apparent comparing with the continuous isolator.

Appendix A. Impedance matrix of the isolator rod

The elements in the impedance matrix $\mathbf{Z}_I$ of the isolator rod [28] in Eq. (20) are expressed as

$$Z_{uy^1Fy^1} = Z_{uy^2Fy^2}$$
$$= -\frac{jE^*Ik_f^3\left[\cos(hk_f)\sinh(hk_f)+\cosh(hk_f)\sin(hk_f)\right]}{\omega\left[1-\cos(hk_f)\cosh(hk_f)\right]}, \tag{A1}$$

$$Z_{uy^1Tx^1} = Z_{\theta x^1Fy^1}$$
$$= -Z_{uy^2Tx^2} = -Z_{\theta x^2Fy^2} = \frac{jE^*Ik_f^2\sin(hk_f)\sinh(hk_f)}{\omega\left[\cos(hk_f)\cosh(hk_f)-1\right]}, \tag{A2}$$

$$Z_{uz^1Fz^1} = Z_{uz^2Fz^2} = -\frac{jE^*Ak_l\cos(hk_f)}{\omega\sin(hk_f)}, \tag{A3}$$

$$Z_{\theta x^1Tx^1} = Z_{\theta x^2Tx^2}$$
$$= \frac{jE^*Ik_f\left[\cos(hk_f)\sinh(hk_f)-\cosh(hk_f)\sin(hk_f)\right]}{\omega\left[1-\cos(hk_f)\cosh(hk_f)\right]}, \tag{A4}$$

$$Z_{uy^1Fy^2} = Z_{uy^2Fy^1}$$
$$= \frac{jE^*Ik_f^3\left[\sin(hk_f)+\sinh(hk_f)\right]}{\omega\left[1-\cos(hk_f)\cosh(hk_f)\right]}, \tag{A5}$$

$$Z_{uy^1Tx^2} = -Z_{\theta x^1Fy^2} = -Z_{uy^2Tx^1} = Z_{\theta x^2Fy^1}$$
$$= \frac{jE^*Ik_f^2\left[\cos(hk_f)-\cosh(hk_f)\right]}{\omega\left[1-\cos(hk_f)\cosh(hk_f)\right]}, \tag{A6}$$

$$Z_{uz^1Fz^2} = Z_{uz^2Fz^1} = \frac{jE^*Ak_l}{\omega\sin(hk_f)}, \tag{A7}$$

$$Z_{\theta x^1Tx^2} = Z_{\theta x^2Tx^1}$$
$$= \frac{jE^*Ik_f\left[\sin(hk_f)-\sinh(hk_f)\right]}{\omega\left[1-\cos(hk_f)\cosh(hk_f)\right]}, \tag{A8}$$

where E^*, I, h, and A respectively denote the complex

Young's modulus, sectional inertia moment, length, and the sectional area of the beam; K_f and k_l are flexural wave number and longitudinal wave number, respectively.

Appendix B. Mobility matrix of the finite plate with constraint boundary

The elements in the mobility matrix $\mathbf{M}_P$ of the finite plate [28] in Eq. (26) are expressed as

$$
\begin{aligned}
m_{uyFy}^{21} = \mathrm{j}\omega \sum_{m=1}^{\infty} \sum_{n=1}^{\infty} \frac{\lambda_{m,n}^{(y)}(x_2,y_2)\lambda_{l,m}^{(y)}(x_1,y_1)}{\varLambda\left[\omega_{lm,n}^2(1+\mathrm{j}\xi)-\omega^2\right]} \\
+\mathrm{j}\omega \sum_{m=0}^{\infty} \sum_{n=0}^{\infty} \frac{\lambda_{m,n}^{(y)}(x_2,y_2)\lambda_{l,m}^{(y)}(x_1,y_1)}{\varLambda\left[\omega_{sm,n}^2(1+\mathrm{j}\xi)-\omega^2\right]},
\end{aligned}
\tag{B1}
$$

$$
m_{uzFz}^{21} = \mathrm{j}\omega \sum_{m=1}^{\infty} \sum_{n=1}^{\infty} \frac{\varphi_{m,n}(x_2,y_2)\varphi_{m,n}(x_1,y_1)}{\varLambda\left[\omega_{fm,n}^2(1+\mathrm{j}\xi)-\omega^2\right]},
\tag{B2}
$$

$$
m_{\theta xFz}^{21} = \mathrm{j}\omega \sum_{m=1}^{\infty} \sum_{n=1}^{\infty} \frac{\psi_{m,n}^{(x)}(x_2,y_2)\varphi_{m,n}(x_1,y_1)}{\varLambda\left[\omega_{fm,n}^2(1+\mathrm{j}\xi)-\omega^2\right]},
\tag{B3}
$$

$$
m_{uzTx}^{21} = \mathrm{j}\omega \sum_{m=1}^{\infty} \sum_{n=1}^{\infty} \frac{\varphi_{m,n}(x_2,y_2)\psi_{m,n}^{(x)}(x_1,y_1)}{\varLambda\left[\omega_{fm,n}^2(1+\mathrm{j}\xi)-\omega^2\right]},
\tag{B4}
$$

$$
m_{\theta xTx}^{21} = \mathrm{j}\omega \sum_{m=1}^{\infty} \sum_{n=1}^{\infty} \frac{\psi_{m,n}^{(x)}(x_2,y_2)\psi_{m,n}^{(x)}(x_1,y_1)}{\varLambda\left[\omega_{fm,n}^2(1+\mathrm{j}\xi)-\omega^2\right]},
\tag{B5}
$$

where $\varLambda = \rho s l_x l_y/4$ is the modal mass; P, s, l_x, and l_y are respectively the density, thickness, length, and width of the plate. The m,nth modal longitudinal wave modal frequencies $\omega_{lm,n}$, shear wave frequencies $\omega_{sm,n}$, and flexural wave $\omega_{fm,n}$ are respectively denoted as

$$
\omega_{lm,n} = \sqrt{\frac{E^*}{\rho(1-v^2)}\left[\left(\frac{m\pi}{l_x}\right)^2+\left(\frac{n\pi}{l_y}\right)^2\right]},
\tag{B6}
$$

$$
\omega_{sm,n} = \sqrt{\frac{G}{\rho}\left[\left(\frac{m\pi}{l_x}\right)^2+\left(\frac{n\pi}{l_y}\right)^2\right]},
\tag{B7}
$$

$$
\omega_{fm,n} = \sqrt{\frac{E^*s^2}{12\rho(1-v^2)}\left[\left(\frac{m\pi}{l_x}\right)^2+\left(\frac{n\pi}{l_y}\right)^2\right]},
\tag{B8}
$$

and $\varphi_{m,n}$, $\lambda_{m,n}^{(x)}$, $\lambda_{m,n}^{(y)}$, $\psi_{m,n}^{(x)}$, and $\psi_{m,n}^{(y)}$ are the m,nth eigenfunctions,

$$
\varphi_{m,n}(x,y) = \sin\frac{m\pi x}{l_x}\sin\frac{n\pi y}{l_y},
\tag{B9}
$$

$$
\lambda_{m,n}^{(x)}(x,y) = \cos(m\pi x/l_x)\sin(n\pi y/l_y),
\tag{B10}
$$

$$
\lambda_{m,n}^{(y)}(x,y) = \sin(m\pi x/l_x)\cos(m\pi y/l_y),
\tag{B11}
$$

$$
\psi_{m,n}^{(x)}(x,y) = \frac{n\pi}{l_y}\sin\frac{m\pi x}{l_x}\cos\frac{n\pi y}{l_y},
\tag{B12}
$$

$$
\psi_{m,n}^{(y)}(x,y) = -\frac{m\pi}{l_x}\cos\frac{m\pi x}{l_x}\sin\frac{n\pi y}{l_y},
\tag{B13}
$$

where E^*, G, v, and ξ are respectively the complex Young's modulus, shear modulus, Poisson's ratio, and loss factor of the plate [30].

1   C. Liu, X. Jing, S. Daley, and F. Li, Recent advances in micro-vibration isolation, Mech. Syst. Signal Process. **56-57**, 55 (2015).
2   M. Harrison, A. O. Sykes, and M. Martin, Wave effects in isolation mounts, J. Acoust. Soc. Am. **24**, 62 (1952).
3   Y. Zhang, J. R. Zhang, and S. J. Xu, Influence of flexible solar arrays on vibration isolation platform of control moment gyroscopes, Acta Mech. Sin. **28**, 1479 (2012).
4   Z. Zhang, H. Ding, Y. W. Zhang, and L. Q. Chen, Vibration suppression of an elastic beam with boundary inerter-enhanced nonlinear energy sinks, Acta Mech. Sin. **37**, 387 (2021).
5   J. Liu, X. Li, and M. Xia, A dynamic model for the planetary bearings in a double planetary gear set, Mech. Syst. Signal Process. **194**, 110257 (2023).
6   J. Liu, H. Ni, R. Zhou, X. Li, Q. Xing, and G. Pan, A simulation analysis of ball bearing lubrication characteristics considering the cage clearance, J. Tribol. **145**, 044301 (2023).
7   X. Li, J. Liu, S. Ding, Y. Xu, Y. Zhang, and M. Xia, Dynamic modeling and vibration analysis of double row cylindrical roller bearings with irregular-shaped defects, Nonlinear Dyn. **112**, 2501 (2024).
8   M. A. Beijen, M. F. Heertjes, H. Butler, and M. Steinbuch, Disturbance feedforward control for active vibration isolation systems with internal isolator dynamics, J. Sound Vib. **436**, 220 (2018).
9   B. Yan, M. J. Brennan, S. J. Elliott, and N. S. Ferguson, Active vibration isolation of a system with a distributed parameter isolator using absolute velocity feedback control, J. Sound Vib. **329**, 1601 (2010).
10   Y. Du, R. A. Burdisso, E. Nikolaidis, and D. Tiwari, Effects of isolators internal resonances on force transmissibility and radiated noise, J. Sound Vib. **268**, 751 (2003).
11   P. G. Dylejko, I. R. MacGillivray, S. M. Moore, and A. T. Skvortsov, The influence of internal resonances from machinery mounts on radiated noise from ships, IEEE J. Ocean. Eng. **42**, 399 (2017).
12   N. B. Roozen, D. Urbán, E. A. Piana, and C. Glorieux, On the use of dynamic vibration absorbers to counteract the loss of sound insulation due to mass-spring-mass resonance effects in external thermal insulation composite systems, Appl. Acoust. **178**, 107999 (2021).
13   E.I. Rivin, Passive Vibration Isolation (ASME Press, New York,

Y. Liu, *et al. Acta Mech. Sin.*, Vol. 41, 523535 (2025)

523535-17

2003).

14 A. Vogel, J. Arnold, C. Voelker, and O. Kornadt, Applicability of the structure-borne sound source characterisation Two-Stage method as well as the parameters derived in sound pressure level predictions in lightweight constructions, Appl. Acoust. **205**, 109242 (2023).

15 A. Baxy, R. Prasad, and A. Banerjee, Elastic waves in layered periodic curved beams, J. Sound Vib. **512**, 116387 (2021).

16 J. V. Sánchez-Pérez, D. Caballero, R. Mártinez-Sala, C. Rubio, J. Sánchez-Dehesa, F. Meseguer, J. Llinares, and F. Gálvez, Sound attenuation by a two-dimensional array of rigid cylinders, Phys. Rev. Lett. **80**, 5325 (1998).

17 Y. Jin, X. Y. Jia, Q. Q. Wu, X. He, G. C. Yu, L. Z. Wu, and B. Luo, Design of vibration isolators by using the Bragg scattering and local resonance band gaps in a layered honeycomb meta-structure, J. Sound Vib. **521**, 116721 (2022).

18 R. Prasad, and A. Sarkar, Broadband vibration isolation for rods and beams using periodic structure theory, J. Appl. Mech. **86**, 021004 (2018).

19 J. Wang, and C. M. Mak, Adaptive-passive vibration isolation between nonrigid machines and nonrigid foundations using a dual-beam periodic structure with shape memory alloy transverse connection, J. Sound Vib. **333**, 6005 (2014).

20 L. J. Wu, and H. W. Song, Band gap analysis of periodic structures based on cell experimental frequency response functions (FRFs), Acta Mech. Sin. **35**, 156 (2019).

21 X. An, C. Lai, W. He, and H. Fan, Three-dimensional meta-truss lattice composite structures with vibration isolation performance, Extreme Mech. Lett. **33**, 100577 (2019).

22 C. Li, T. Jiang, Q. He, and Z. Peng, Stiffness-mass-coding metamaterial with broadband tunability for low-frequency vibration isolation, J. Sound Vib. **489**, 115685 (2020).

23 M. Hajhosseini, and Z. Zeinalizadeh, New periodic lattice model with specific vibration absorption patterns at resonant frequencies, Acta Mech. Sin. **39**, 522463 (2023).

24 W. Sun, D. Thompson, and J. Zhou, A mechanism for overcoming the effects of the internal resonances of coil springs on vibration transmissibility, J. Sound Vib. **471**, 115145 (2020).

25 Y. Du, R. A. Burdisso, and E. Nikolaidis, Control of internal resonances in vibration isolators using passive and hybrid dynamic vibration absorbers, J. Sound Vib. **286**, 697 (2005).

26 P. G. Dylejko, and I. R. MacGillivray, On the concept of a transmission absorber to suppress internal resonance, J. Sound Vib. **333**, 2719 (2014).

27 J. Szefi, E. Smith, and G. Lesieutre, in Design and analysis of high-frequency periodically layered isolators for helicopter gearbox isolation: Proceedings of the 44th AIAA/ASME/ASCE/AHS Structures, Structural Dynamics, and Materials Conference, Norfolk, 2003. 784.

28 P. Gardonio, S. J. Elliott, and R. J. Pinnington, Active isolation of structural vibration on a multiple-degree-of-freedom system, Part I: The dynamics of the system, J. Sound Vib. **207**, 61 (1997).

29 J. F. Doyle, Wave Propagation in Structures, 3rd ed. (Springer, Cham, 2021).

30 M. Östberg, M. Coja, and L. Kari, Dynamic stiffness of hollowed cylindrical rubber vibration isolators—The wave-guide solution, Int. J. Solids Struct. **50**, 1791 (2013).

基于非周期隔振器的一种内共振抑制及优化方法

刘玉君, 刘静, 潘光, 黄桥高, 宋保维

摘要 隔振器的内共振会明显影响其在中高频段的隔振性能, 周期隔振器具有良好的中高频滤波特性, 但内共振效应依然存在, 尤其是在隔振器阻尼较小的情况下. 为了降低周期隔振器的内共振影响, 本文提出了一种新型非周期隔振器. 首先解释了基于非周期隔振器的内共振控制机理; 通过子系统法和传递矩阵法, 推导了电机、非周期隔振器和弹性支撑板耦合的动力学模型, 采用有限元方法验证了数值模型的准确性, 数值分析了隔振器的非周期性和阻尼对内共振的抑制效果. 结果表明, 在中高频段, 周期隔振系统和非周期隔振系统的隔振性能明显优于连续隔振系统. 与能带结构中滤波通带周期性存在的周期隔振器相比, 非周期隔振器打开了能带结构中的通带带隙. 结果表明含阻尼的周期隔振器和非周期隔振器都具有能带结构加宽效应. 为了提高内共振的控制效果, 提出了一种非周期隔振器参数优化方法, 优化后的非周期隔振器在目标频带内的内共振峰值得到了有效的降低. 最后, 基于实验方法对三种不同的隔振系统的隔振性能进行了测试.